Supporting Information for

The obscuring effect of magma recharge on the connection of volcanic-plutonic rocks

K. Zhao[1], X. S. Xu[1], Z. Y. He[2], and Y. Xia[1]

[1]State Key Laboratory for Mineral Deposits Research, School of Earth Sciences and Engineering, Nanjing University, Nanjing 210023, China

[2]School of Civil and Resource Engineering, University of Science and Technology Beijing, Beijing 100083, China

Text S1. Homogenization techniques of crystallized melt inclusions

Completely crystallized melt inclusions are observed in the Banba rhyolite. Homogenization of the crystallized melt inclusions follows the protocol of Student & Bodnar (1999, 2004). Quartz phenocrysts containing melt inclusions were picked out, placed in a Pt holder and incrementally heated in a 1 atm muffle furnace. The homogenization temperature is predicted to be ~900-1000 °C by reconnaissance thermodynamic modeling with 1-3 wt% initial H_2O contents. Therefore, the quartz phenocrysts were initially placed in the furnace and incrementally heated at 30 °C/minute from room temperature to 500 °C, and the sample was then heated at a rate of ~1 °C/minute to ~900 °C. Afterwards, the heated quartz was rapidly quenched in water at a rate >800 °C/s and then observed with a petrographic microscope on epoxy mounts to examine whether the inclusions were totally homogenized. If not, the procedure was repeated with a 10 °C increase in final temperature until the quenched inclusions contained only a single glass

phase. Melt inclusions greater than ~20 μm may decrepitate and leak during heating. To eliminate the decrepitation problem, the hand specimen sample was also heated following the above procedure and then cut into double polished thin sections for observation under a microscope. Those parts of the thin sections containing glass inclusions were cut off and mounted in epoxy. Finally, the homogenized melt inclusions in both the mounted quartz and thin-section pieces were polished to the surface for further analyses.

Text S2. Mineral composition imaging

Back-scattered electron (BSE) images were obtained on polished thin sections using a JEOL JXA-8800 electron microprobe at the State Key Laboratory for Mineral Deposits Research (LAMD) at Nanjing University, China. Zircon and quartz cathodoluminescence (CL) was mostly obtained using a SUPRA 55 SAPPHIRE scanning electron microscope (SEM) located at the LAMD, and part of the quartz CL imaging was performed using a Tescan MIRA3 LM instrument equipped with a CL detector in Hongchuang Geological Services Ltd. The BSE intensity correlates with a greater average atomic number of the sample, and CL zones are defined by variations in luminosity due to differences in trace elements (e.g., Ti) and defect abundances within the crystal structure (Barbee et al. 2019; Tavazzani et al. 2020). We further extracted grayscale data from the CL-based images using ImageJ software and examined the correlation between the grayscale and Ti contents.

Mineral phase maps (Fig. 3a, b in the main text) were obtained on carbon-coated thin sections using a Mira-3 scanning electron microscope equipped with four energy dispersive X-ray spectroscopy (EDS, EDAX Element 30) at Nanjing Hongchuang Geological Exploration Technology Service Co., Ltd. We use an acceleration voltage of 25 kV, probe current of 9 nA. Working distance was set to 15mm. Pixel spacing was set to 3μm and dot

spacing was set to 9μm. The current and BSE signal intensity were calibrated on a platinum Faraday cup using the automated procedure. EDS performance was checked using manganese standard. The samples were scanned using TIMA liberation analysis module. Micro X-ray fluorescence spectrometer (Bruker/M4 Tornado) was also used to obtain mineral phase maps (Fig. 2f in the main text) and analyze the composition of groundmass. This instrument has 10 μm spatial resolution with a mono capillary lens and a Rh target X-ray tube (50 kV, 600 μA). The sample chamber was in vacuum. The analyses typically cover areas of larger than 500 μm × 500 μm and depths of <100 μm.

Text S3. Mineral and melt inclusion geochemical analyses

Major elements (Si, Ti, Al, Fe, Mn, Mg, Ca, Na, K) of plagioclase, alkali feldspar, titanite and melt inclusions (F and Cl analysed) were acquired using a JEOL JXA-8230 electron microprobe at LAMD, Nanjing University. For analyses of minerals, we used a beam size of 1-5 μm, an accelerating potential voltage of 15 kV, and a probe current of 15 nA. Peak and background counting times were 10 s and 5 s for major and trace elements, respectively. Natural hornblende (Si, Ti, Al, Fe, Ca, Na, K), fayalite (Mn), and synthetic compounds (albite, anorthite and orthoclase) were used as standards. For analyses of melt inclusions in the Banba rhyolite, we used a probe current of 2-4 nA and a defocused beam size of 5-10 μm to minimize the problem of Na loss. An obsidian glass from Lake Country, Oregon, is used to monitor the quality of data. Analyses of the obsidian glass yielded results that are overall consistent with recommended values within ±2σ (Supplementary Table S2), but systematic offsets of Na_2O, Al_2O_3 and SiO_2 data with decreasing beam size are observed, and a linear or polynomial fit strategy was thus employed to correct the offset. Matrix

effects were automatically corrected using JEOL ZAF software. The analytical accuracy was 1%-5%.

Quartz trace elements of the volcanic and plutonic rocks were analysed with laser ablation inductively coupled plasma–mass spectrometry (LA-ICP MS) at LAMD, Nanjing University. Analyses were conducted on polished thin sections (>100 μm thick) and epoxy mounts using a Thermo-Finnigan Element 2 sector field ICP–MS coupled with a 193 nm ArF Excimer laser (GeolasPro system, Coherent, USA). The laser was fired at a repetition rate of 10 Hz, the laser energy was 20 J/cm^2, and the beam size was 60 μm. The ablated material was transported by high purity He gas from the laser ablation cell at a flow rate of 0.5 l/min. Before analysis, the ICP–MS was tuned to achieve maximum sensitivity and a low oxide production rate by lowering the ThO/Th ratios to <0.5%. The acquisition time for each analysis was 60 s, including 20 s for background scanning. Analysed isotopes include ^{7}Li, ^{23}Na, ^{24}Mg, ^{27}Al, ^{29}Si, ^{31}P, ^{39}K, ^{43}Ca, ^{49}Ti, ^{55}Mn, ^{57}Fe, ^{85}Rb, ^{88}Sr, ^{89}Y, ^{137}Ba, ^{139}La, and ^{140}Ce, with ^{29}Si as the internal standard. Isotopes were measured using dwell times of 10 to 30 ms per isotope. Data acquisition was in blocks of up to 15 measurements, with NIST 610 analysed twice at the beginning and at the end. NIST 612 was used as a quality control reference material. The analysed results of NIST 610 and 612 (reported in Supplementary Table S1) were consistent with the recommended values within ±2σ.

Zircon trace elements of the volcanic and plutonic rocks were analysed with the LA-ICP MS method using the same facilities as the analysis of quartz trace elements in the LAMD but with different parameters during analysis. The laser was fired at a repetition rate of 5 Hz, the laser energy was reduced to 7 J/cm^2, and the beam size was 32 μm. The acquisition time for each analysis was 80 s, including 20 s for background scanning.

Analysed isotopes include ^{29}Si, ^{31}P, ^{49}Ti, ^{89}Y, ^{91}Zr, ^{93}Nb, ^{139}La, ^{140}Ce, ^{141}Pr, ^{143}Nd, ^{147}Sm, ^{151}Eu, ^{155} Gd, ^{159}Tb, ^{163}Dy, ^{165}Ho, ^{166}Er, ^{169}Tm, ^{173}Yb, ^{Lu}175, ^{179}Hf, ^{181}Ta, ^{202}Hg, ^{204}Pb, ^{206}Pb, ^{207}Pb, ^{208}Pb, ^{232}Th, and ^{238}U. Such a setting allows us to simultaneously yield the U–Pb age of the analysed spot. Calibration of trace elements was performed using NIST standard glass 612 (Pearce et al. 1997) with ^{29}Si as the internal standard (see Supplementary Table S1).

Text S4. Whole-rock major- and trace-element compositional analysis

Whole-rock major-element of the Taima and Dasi porphyries, and the late Jiuzhou pluton has been reported in Zhao et al. (2017b) (see the supplementary Table. S2.). Here, whole-rock major-element analysis of three rhyolite and two tuff samples from the Banba formation and two monzogranite from the early Jiuzhou pluton were performed using an ARL9800XP+ X–ray fluorescence spectrometer (XRF) at the State Key Laboratory of Mineral Deposits Research, Nanjing University. Glass discs were prepared by fusing a mixture of sample powder with an alkali flux (consisting of a 66.33: 33.17: 0.5 mixture of lithium tetraborate, lithium metaborate and lithium bromide at 1050 °C). Analyses were carried out with an accelerating voltage of 50 kV and a beam current of 50mA. Standards (GSR–3) were prepared using the same procedure to monitor analytical precision, which is generally better than 2%. Whole-rock major element analyses of samples JZ01-2, JZ02-3, and DS04-2 were performed using an ARL9800XP + X-ray fluorescence spectrometer (XRF) at the Center of Modern Analysis, NJU. The analytical precision is generally better than 2%.

Trace-element analyses of most samples were undertaken at the State Key Laboratory of Mineral Deposit Research, Nanjing University. For trace-element analyses, ca. 50 mg

of powder was dissolved in high–pressure Teflon bombs using a HF + HNO3 mixture. Rh was used as an internal standard to monitor signal drift during ICP–MS analyses. Trace-element concentrations were determined using a Finnigan Element II ICP–MS. The precision of ICP–MS analyses is <10% for all trace elements and <5% for most of them.

Text S5. Whole-rock Sr-Nd isotopic analysis

Whole-rock Sr-Nd isotopic analysis of the Taima and Dasi porphyries, and the late Jiuzhou pluton has been reported in Zhao et al. (2017b), which is provided in the supplementary Table. S2. New Sr-Nd isotopic data are reported for two rhyolite and two tuff samples from the Banba formation and two monzogranite from the early Jiuzhou pluton. Sr isotopic composition was measured using a Finnigan Triton TI thermal ionisation mass spectrometer (TIMS) at the State Key Laboratory of Mineral Deposits Research, Nanjing University. Nd isotopic composition was measured using the Neptune (Plus) MC–ICP–MS at the State Key Laboratory of Mineral Deposits Research, Nanjing University. For whole-rock Sr–Nd isotopic analysis, ca. 50 mg of powder was dissolved in the same procedure as for the trace-element analyses. Rb–Sr and Sm–Nd were separated using AG50W× 8 resin and various eluents. The rare earth elements (REEs) were first separated from Rb–Sr by conventional cation exchange chromatography using HCl as an eluent. Rb and Sr were then separated and purified using a mixed eluent of pyridinium and DCTA complex. Sm and Nd were separated and purified using HIBA as an eluent through a small volume of cation exchange resin (0.6 mL). $^{87}Sr/^{86}Sr$ and $^{143}Nd/^{144}Nd$ ratios are reported as analyzed, after normalization to $^{86}Sr/^{88}Sr = 0.1194$ and $^{146}Nd/^{144}Nd = 0.7219$ (O'Nions et al. 1977), respectively, to correct for instrumental fractionation. The long-term measurements of the Japan JNdi–1 Nd standard yielded $^{143}Nd/^{144}Nd = 0.512096 \pm 0.000008$ (2σ) and $^{87}Sr/^{86}Sr=$

0.710248 ± 0.000004 (2σ) for NIST SRM 987 Sr standard. For the calculation of $(^{87}Sr/^{86}Sr)_i$, $\varepsilon_{Nd}(t)$ and Nd model ages, the following parameters were used: $\lambda_{Rb}=1.42\times10^{-11}$ year^{-1} (Minster et al. 1982); $\lambda_{Sm}=6.54\times10^{-12}$ year^{-1} (Lugmair and Marti 1978); $(^{147}Sm/^{144}Nd)_{CHUR}=0.1960\pm4$, $(^{143}Nd/^{144}Nd)_{CHUR}=0.512630\pm11$ (2σ) (Bouvier et al. 2008); $(^{143}Nd/^{144}Nd)_{DM}=0.513151$, $(^{147}Sm/^{144}Nd)_{DM}=0.2136$ (Liew and Hofmann 1988).

Text S6 Whole-rock oxygen isotopic analysis

Whole-rock oxygen isotopic analysis for three rhyolite sample from the Banba formation, two samples from Taima porphyry and two samples from the Dasi porphyry were conducted in ALS Minerals Laboratory, Guangzhou, China. Oxygen Isotope values are measured according to the conventional BrF5 procedure of Clayton and Mayeda (1963) and analyzed on a Finnigan MAT 252 isotope-ratio mass spectrometer (IRMS). Approximately 5mg of mineral separate were reacted with BrF5 at ca. 550~600℃ overnight. The extracted oxygen was converted to CO_2 in contact with a heated graphite rod and the CO_2 was then analyzed off-line using a Finnigan MAT 252 isotope ratio mass spectrometer (IRMS). The results are given in the customary $\delta^{18}O$ notation, relative to Vienna standard mean ocean water (V-SMOW). The typical uncertainty for reproducibility of $\delta^{18}O$ measurements based on repeat measurements of reference materials is <±0.3‰.

Text S7. Methods of diffusion modeling

Intracrystalline diffusion of Ti in zoned quartz crystals affords an effective approach to yield constraints on the timescale of magmatic processes (e.g., Gualda et al. 2012b; Jollands et al. 2020; Tavazzani et al. 2020). The diffusivity of Ti in quartz has been

calibrated by different studies, and recent calibrations (Jollands et al. 2020; Audétat et al. 2021) yield much lower diffusivities than earlier calibrations (Cherniak et al. 2007).

The widely used diffusivity calibration of Ti in quartz comes from annealing experiments at 1 atm, which allow diffusion between polished quartz plates and TiO_2 powder or polished rutile (Cherniak et al. 2007). Over the temperature range 700-1150 °C, the following Arrhenius relation was obtained:

$$D_{\mathrm{Ti}} = D_0 \exp(\frac{E}{RT}), \qquad (1)$$

where E is the activation energy (273000 J mol^{-1}), D_0 is the diffusivity of Ti (7×10^{-8} m^2 s^{-1}), R is the universal gas constant (8.1345 J mol^{-1} K^{-1}) and T is Kelvin temperature. Recently, Jollands et al. (2020) used a similar experimental setup but yielded Ti diffusivities that are two to three orders of magnitude lower than the results of Cherniak et al. (2007). The latest calibration by Audétat et al. (2021) obtained from hydrothermal experiments at a wide range of temperatures and pressures further confirms the slow Ti diffusion in quartz, and quantitative data acquired from multiple analytical techniques are fitted by the following linear regression:

$$\mathrm{Log}_{10} D_{\mathrm{Ti}} = -A - B\frac{10000}{T}, \qquad (2)$$

where constants A and B are 11.31 (±0.66) and 1.37 (±0.10), respectively, and T is the Kelvin temperature. In our study, we estimate the diffusive relaxation timescale of Ti in quartz with Equation (2) based on the following considerations. i) The slow Ti diffusion in quartz is confirmed by two independent experiments (Jollands et al. 2020; Audétat et al. 2021), which yield comparable results. ii) Some studies have suggested that the previous calibration by Cherniak et al. (2007) yielded a much shorter timescale in comparison with

constraints from zircon U-Th dating (Chamberlain et al. 2014), while the latest calibrations could yield timescales well match the zircon U–Th dating results (e.g., Jollands et al. 2020). The slow Ti diffusion will yield long timescale of quartz residence in reservoir, which has been fully considered in the discussion in main text.

If the diffusivities at magmatic temperatures of interest are known, the timescale of diffusive relaxation can be calculated using Fick's second law. For a single dimension and for a diffusion coefficient (D_{Ti}) of Ti in quartz that is independent of direction in space (x) or concentration (C), Fick's second law is:

$$\frac{\partial C}{\partial t} = D_{Ti}\frac{\partial^2 C}{\partial x^2} \qquad (3).$$

One of the most common analytical solutions of this equation is:

$$C(x) = \frac{(C_1 - C_2)}{2} erfc\left(\frac{x - x_c}{2\sqrt{D_{Ti}t}}\right) + C_2 \qquad (4).$$

where C_1 and C_2 refer to the initial concentrations of Ti on each side of an initial interface ($x=x_c$), and $L = \sqrt{D_{Ti}t}$ represents the characteristic diffusion length scale as a function of time, t. The analytical solution (Equation 4) is mostly applicable to diffusion in an infinite medium with an initial condition that has constant C_1 and C_2 on each side of the initial interface. For a general initial condition, i.e., $C|_{t=0}=f(x)$, some sort of numerical method is required to solve Equation 1 (such as the finite difference method, FDM, Costa et al. 2008; Jollands et al. 2020). Using FDM, the discretized grid system is modeled as a vector representing a series of equidistant steps (spacing = Δx), with given initial and boundary conditions. The model then steps forward through time (size of time step = Δt), with the concentration (C) at each distance step (i) recalculated at every time step (j):

$$C_{i,j+1} = C_{i,j} + \frac{D\Delta t}{\Delta x^2}(C_{i+1,j} - 2C_{i,j} + C_{i-1,j}) \qquad (5).$$

For stability of the equation system, the size of the time step, $(D\Delta t)/\Delta x^2$, must be less than 0.5. To improve the stability and precision of solutions, the above difference equation can be substituted as follows:

$$2C_{i,j} - 2C_{i,j-1} = \frac{D\Delta t}{\Delta x^2}(C_{i+1,j} - 2C_{i,j} + C_{i-1,j} + C_{i+1,j-1} - 2C_{i,j-1} + C_{i-1,j-1}) \qquad (6).$$

This is the so-called Crank-Nicolson method (Sauer 2011), which is numerically stable at any time step.

The predicted composition profile from the analytical (Equation 2) or numerical (Equation 4) solutions (solved with a MATLAB code) is fit to the observations by adjusting C_1, C_2, and t to minimize the sum of the squares of the differences (SSD) between observed and predicted compositions. Uncertainties of the method are estimated at ~190-215% (Gualda et al. 2012b) using the Ti diffusivity calibration by Cherniak et al. (2007). We further conduct uncertainty analysis for the Audétat et al. (2021) calibration. Equation $L = \sqrt{D_{Ti}t}$ can be rewritten as an explicit function of temperature (T):

$$t = \frac{L^2}{10^{-A-B\frac{10000}{T}}} \qquad (7).$$

The uncertainties can be evaluated by the following error propagation equation:

$$\left(\frac{\sigma_t}{t}\right)^2 = (\ln 10)^2 \left\{ \sigma_A{}^2 + \left(\frac{10000B}{T}\right)^2 \left[\left(\frac{\sigma_B}{B}\right)^2 + \left(\frac{\sigma_T}{T}\right)^2 \right] \right\} + \left(2\frac{\sigma_L}{L}\right)^2 \qquad (8).$$

Uncertainties in the constants σ_A and σ_B are derived from experiments (i.e., σ_A=0.66 and σ_B=0.10), and σ_T is likely on the order of ~55 K for Ti_in_zircon thermometers. Uncertainties in L derive from the fitting procedure, which likely has estimated errors of

ca. 10-50% (Gualda et al. 2012b). With these parameters, the method likely has uncertainties of 210-250% associated with the diffusive relaxation time, which is similar to the previously estimated uncertainties (217-240%; Gualda et al. 2012b; Wu et al. 2022).

Text S8. Petrography of the Jiuzhou granite

The early Jiuzhou monzogranite mainly consists of quartz, plagioclase, alkali feldspar, biotite and cordierite without orthopyroxene. The monzogranite is massive, showing no layering or a preferred fabric under outcrop, hand specimen and micro scale observations. Plagioclase crystals are largely euhedral to subhedral, showing no deformation and shape preferred orientation (SPO). Quartz and alkali feldspar are subhedral to interstitial, and biotite is euhedral to subhedral. The euhedral to subhedral cordierite crystals are altered to sericite and chlorite.

The charnockite of the late Jiuzhou pluton has a mineral assemblage of quartz, alkali feldspar, plagioclase, biotite, orthopyroxene, and cordierite. The charnockite shows a weak preferred fabric on the handspecimen and microscale, i.e., the euhedral to subhedral plagioclase crystals are mutually in contact forming monomineralic clusters and chains, and some of the crystals show ductile deformation features, e.g., undulose extinction, mechanical twins, subgrains, and/or slightly bent crystals (see more detailed descriptions in Zhao et al. 2018). The orthopyroxene-free granites of the late Jiuzhou pluton are medium-grained with maximum crystal sizes of <3-5 mm. Compared with the charnockite, the orthopyroxene-free granites are plagioclase- and biotite-poor, but quartz- and alkali-feldspar-rich. Plagioclase crystals show a random to slightly clustered distribution without apparent deformation (e.g., mechanical twinning or subgrains). Alkali feldspar crystals are

subhedral to poikilitic. Biotite crystals are euhedral to subhedral. Cordierite crystals are euhedral to subhedral, which are partly altered to fine-grained sericite and chlorite.

Text S9. P-T constraints combining thermodynamic modeling and thermometry

Banba rhyolite

The reactive magma composition for the Banba rhyolite is reconstructed by subtracting compositions of out-of-equilibrium phenocrysts (OEPs). The out-of-equilibrium quartz crystals are represented by Groups B and C quartz, which are estimated to account for ~25% of the quartz phenocryst population (~5.5 vol%) on the basis of statistics of CL images. As plagioclase is significantly altered, it is hard to obtain the primary composition and estimate the out-of-equilibrium fraction. We assume that plagioclase has ~50-60 mol% anorthite contents and ~25% of the plagioclase phenocryst population (~9.1 vol%) is out of equilibrium. The assumption has little influence on the reactive magma composition due to the low fraction of phenocrysts (see Table S1).

The Banba melt inclusions likely have H_2O contents of 2.5 wt% on average, as inferred from volatiles by the difference method (see supplementary Table. S2). If the bulk magma contains ingredients such as accumulated crystals, more mafic magma and/or resitite, the mixture would be less hydrous. We thus test different system H_2O contents of 1.0 wt%, 1.5 wt% and 2.0 wt% to examine how the phase relationships vary accordingly. Irrespective of pressure, plagioclase is the liquidus phase at ~1000 °C, ~980 °C and ~960 °C at 1.0 wt%, 1.5 wt% and 2.0 wt% initial H_2O contents, respectively (Fig. 9a, b, c). Orthopyroxene crystallizes at ~900-870 °C at 1.5-2.0 wt% initial H_2O contents, which is earlier than quartz within the considered pressure conditions (Fig. 9b, c) but becomes later

than quartz at 1.0 wt% initial H_2O content and >70 MPa (Fig. 9a). This is because the higher initial H_2O content will shrink the stability field of quartz from ~890-940 ℃ at 1.0 wt% initial H_2O content (Fig. 9a), over ~840-890 °C at 1.5 wt% initial H_2O content (Fig. 9b), to ~800-850 ℃ at 2.0 wt% initial H_2O content (Fig. 9c). Alkali feldspar saturates later than quartz, and the stability field of alkali feldspar is also influenced by H_2O content, i.e., the saturation temperature decreases from 860-890 °C at 1.0 wt% H_2O content (Fig. 9a), over 825-855 °C at 1.5 wt% H_2O content (Fig. 9b), to 800-840 °C at 2.0 wt% H_2O content (Fig. 9c). Biotite is predicted to saturate at ~750-770 ℃ irrespective of H_2O contents but only presents at pressures >90 MPa (Fig. 9). Cordierite is not present because the aluminum saturation index (1.08) of the average composition used in the modeling may not be sufficiently high to stabilize cordierite. The initial melt H_2O content also apparently shifts magma crystallinity to lower temperatures, i.e., the Banba rhyolite with <20 vol% crystallinities corresponds to temperatures of >850-880 °C at 1 wt% H_2O content, >820-845 °C at 1.5 wt% H_2O content, and >780-820 °C at 2 wt% H_2O content.

Combined with the results of thermodynamic modeling, we can judge whether the calculated Ti_in_zircon temperatures at different $aTiO_2$ reasonably represent the crystallization temperature of magma. For the Banba rhyolite, at an $aTiO_2$ of 0.75, the Ti_in_zircon temperature is such low that it could stabilize alkali feldspar, and the magma quenches at high crystallinities (>40-60 vol%) assuming initial H_2O contents of 1-1.5 wt% (Fig. 9a, b), which is not consistent with the petrographic observations of the Banba rhyolite. Higher H_2O contents (≥2 wt%) may shift the stability field of alkali feldspar and the crystallinity isopleth to lower temperatures, but quartz cocrystallizes with alkali feldspar in this case, which is not observed in our sample (Fig. 9c). At an $aTiO_2$ of 0.5, the

higher Ti_in_zircon temperature corresponds to relatively low crystallinities in the pressure interval of 50-100 MPa, e.g., 40-45 vol% at 1 wt% H_2O (Fig. 9a), 15-20 vol% at 1.5 wt% H_2O (Fig. 9b), and <10 vol% at 2 wt% H_2O content (Fig. 9c). The case of initial 1.5 wt% H_2O content seems to be approximate to the observed <19 vol% phenocryst fraction, and the temperature interval of zircon crystallization overlaps little with the stability field of alkali feldspar (Fig. 9b), consistent with the absence of alkali feldspar in our sample. Therefore, the Ti_in_zircon temperature at an $aTiO_2$ of 0.5 agrees well with the thermodynamic-based phase relationship for the Banba rhyolite.

Taima porphyry

For the crystal-rich porphyries, the out-of-equilibrium phenocrysts (OEPs) are also dominated by cores of zoned quartz (Group C) and plagioclase. Other phenocrysts (alkali feldspar, orthopyroxene, biotite, and cordierite) are largely homogeneous (Zhao et al. 2017a) and thus represent equilibrium phenocrysts with the interstitial melts. Average modal contents of the Taima porphyry are around 13.2% for quartz phenocrysts and 13.6% for plagioclase phenocrysts (see Table S1). Statistics of quartz CL and plagioclase BSE images suggest OEPs account for ~20 % of quartz and plagioclase phenocrysts. Thermodynamic modeling with variable amounts of OEPs suggests that the measured compositional distribution of plagioclase phenocrysts could be best fitted by excluding ~20-30% OEPs from the average composition (Fig. 13c). The reconstructed reactive magma composition is slightly different from the average whole-rock composition of the Taima porphyry (with 71.0 wt% versus 72.3 wt% SiO_2, respectively; Table S1). Such a difference leads to a small difference in phase relations, i.e., the modeling using reactive

magma composition predicts that quartz and alkali feldspar saturate at slightly higher (<10 °C) temperatures, yet the stability fields of plagioclase, orthopyroxene, biotite, and cordierite shift to slightly lower (10-20 °C) temperature, compared to the modeled phase relations using average whole-rock composition (Fig. S11). In the following, phase relations of the reactive magma are described in detail.

Thermodynamic modeling results are shown at a pressure range of 30-200 MPa. The initial melt H_2O content is considered at 1.0 wt%, 1.5 wt% and 2.0 wt%, but for the case of 1.0 wt% H_2O content, the alkali feldspar is predicted to saturate at ~900 °C at 200 MPa, which is inconsistent with the previous two-feldspar thermometric result at ~830±50 °C at 200 MPa (Zhao et al. 2017a). We thus only show the results at 1.5 wt% and 2.5 wt% H_2O contents (Fig. 10). The modeling suggests that plagioclase, orthopyroxene, and cordierite are the earliest phases crystallized at >870 °C (Fig. 10). The saturation temperatures of quartz and alkali feldspar are influenced by the initial H_2O contents, i.e., the temperatures decrease from 825-900 °C to 780-850 °C for quartz and from 820-860 °C to 780-830 °C for alkali feldspar (Fig. 10) with initial H_2O content increasing from 1.5 wt% to 2.0 wt%, respectively. Biotite is predicted to saturate at <750 °C and >85 MPa at all considered H_2O contents (Fig. 10). The 29-54 vol% crystallinities of the Taima and Dasi porphyric magmas correspond to temperatures of >780-800 °C at 1.5 wt% H_2O content and >745-775 °C at 2 wt% H_2O content.

For the Taima magmas, at an $aTiO_2$ of 0.75, the Ti_in_zircon temperatures of 765-810 °C are too low to stabilize orthopyroxene (Fig. 10a, b). At an $aTiO_2$ of 0.5, the higher Ti_in_zircon temperatures of 805-855 °C comply well with the phase relationship in the case of 1.5 wt% H_2O, where all major phases (quartz, plagioclase, alkali feldspar,

orthopyroxene and cordierite) are stable (Fig. 10a) and the corresponding crystallinities of 20-50 vol% are also consistent with the observation (28-54%), while at 2.0 wt% H_2O, the predicted crystallinities of <30 vol% (Fig. 10b) in the pressure interval of 50-200 MPa are too low, and more importantly, the stability fields of quartz and alkali feldspar are very narrow. Therefore, the Ti_in_zircon temperature of 830±24 °C (835±29 °C) at an $aTiO_2$ of 0.5 is more representative of the Taima and Dasi porphyries.

Text S10. Relating $\delta^{18}O_{(Zrc)}$ to $\delta^{18}O_{(WR)}$

Assuming that the minerals approach isotopic equilibrium at the magmatic stage (on the basis of the protracted residence timescale, see main text), isotopic fractionation factors at a given temperature are expressed as

$$\Delta_{i-j} = \delta^{18}O(\text{mineral}-i) - \delta^{18}O(\text{mineral}-j) \approx 1000\ln\alpha(\text{i}-\text{j}) \approx \frac{A_{i-j}\times 10^6}{T^2} \quad (9)$$

where T is temperature (K) and A is an experimentally or empirically determined coefficient (Zhao and Zheng 2003; Bindeman, 2008). Using the modal abundance of the Sierra Nevada granites and the published equilibrium fractionation factors for various minerals, Lackey et al. (2008) derived the following relationship linking whole-rock and zircon $\delta^{18}O$ data as a function of SiO_2 content:

$$\Delta^{18}O(\text{WR}-\text{Zrc}) \approx 0.0612(\text{SiO}_2\,\text{wt}\,\%) - 2.50 \pm 0.36‰ \quad (10)$$

Following this relationship, whole-rock $\delta^{18}O$ values could be calibrated upward by ~1.78-2.03±0.36‰ on the basis of the zircon $\delta^{18}O$ values at 70-74 wt% SiO_2 for the Banba rhyolite and the Taima and Dasi porphyries. However, the above relationship was derived at the magma solidus temperature (~700 °C at 70-74 wt% SiO_2; Lackey et al. 2008), which

may be applicable for granite plutons. For volcanic magmas quenched at higher temperatures (e.g., ~855 °C for the case of the Banba rhyolite, Fig. 9a), the calibration values between whole-rock and zircon $\delta^{18}O$ data should be lower (see Equation 9). We thus calibrate the zircon $\delta^{18}O$ data by 1.3-1.5±0.36‰ at 800-850 °C.

Text S11. Fractionation modeling and mass balance calculation

The modelling procedure is based on the mass balance calculation, which has been widely used in published papers with modifications (e.g., Zhao et al. 2018; Farina et al. 2020). In the main text, the fractionation trend of the Banba rhyolite is best represented by the compositional variation of the melt inclusion, as suggested by the consistent variation trend with the thermodynamic modelling (see Fig. 9 in the main text). We thus could use the melt inclusion composition to represent the interstitial melt composition, and the cumulate mineral compositions could be calculated based on mass balance using the least evolved melt inclusion as parental magma. The disadvantage of the procedure is that we do not know the crystallinity of each incremental step. We thus simplify the modelling procedure as a first-order approximation. Thermodynamic modelling suggests that the melt inclusion compositions cluster at ~74-76 wt% SiO_2 at 50-60% crystallinities. The average composition of these melt inclusions is thus used to represent the interstitial melt composition, and the composition of pure cumulate (without interstitial melting) is calculated at ~65 wt% SiO_2. The fractionation trend is calculated considering the interstitial composition plus a variable (0-30 wt%) unsegregated pure cumulate component. We note here that this simplification only affects the absolute values but not the compositional vectors and our general conclusions.

We further conduct mass balance calculations to quantitatively examine whether the combination of recharge and fractionation processes could account for the variation in whole-rock composition. The effect of magma recharge is modelled by incrementally increasing the proportions (5-25%) of recharge magmas on the basis of unsegregated phenocryst fractions of 0-30% (Fig. 13). The composition of the recharge magma is represented by the dacite in the northwestern QBGC (Qin et al. 2011). As shown in Fig. 13, the mass balance calculation suggests that the results considering recharge and fractionation processes roughly reproduce the bulk compositions of the Banba rhyolite (Fig. 13), except that the modelled Al_2O_3, Fe_2O_3, and MgO contents are slightly lower by ~1 wt% (Fig. 13a), ~0.8 wt% (Fig. 13b) and ~0.5 wt% (Fig. 13c), respectively.

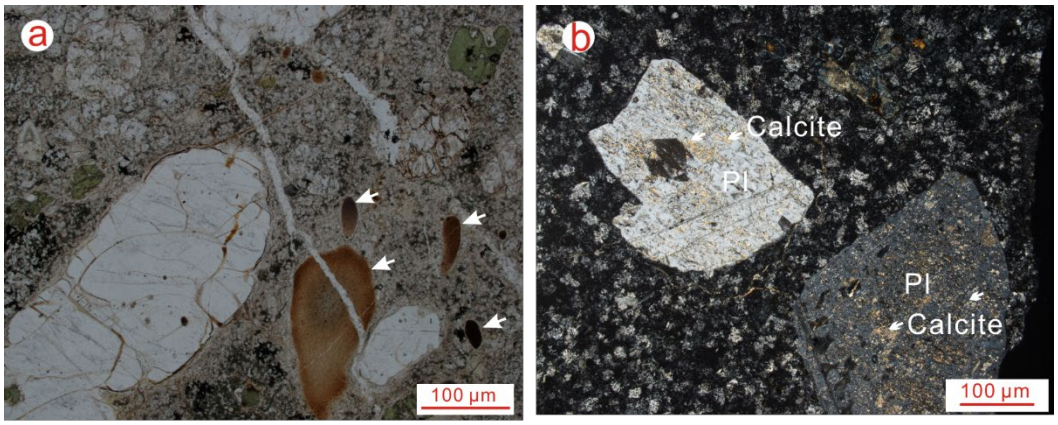

Fig. S1 (a) Petrographic photo showing xenolithic materials (the dark brown and opaque grains shown by arrows) in Sample BB02-1, which is likely entrained during eruption and deposition processes; (b) Carbonatation of plagioclase phenocrysts.

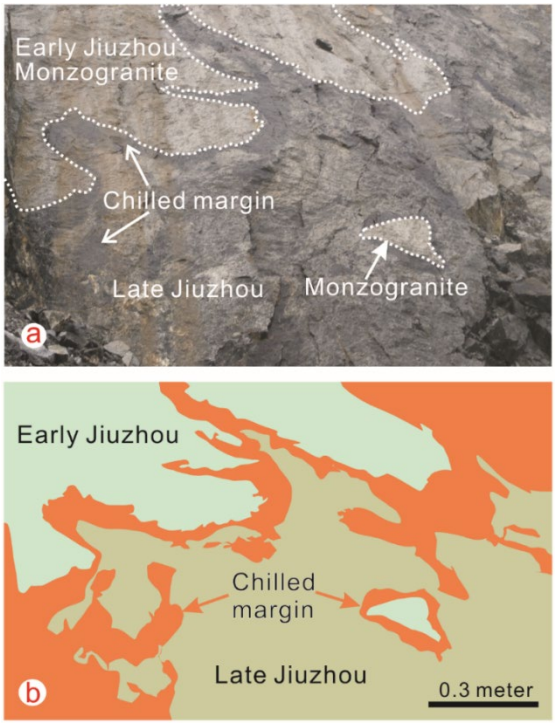

Fig. S2 Field observation (a) and sketch figure (b) outlining the intrusive relationship of the early and late phases of the Jiuzhou pluton.

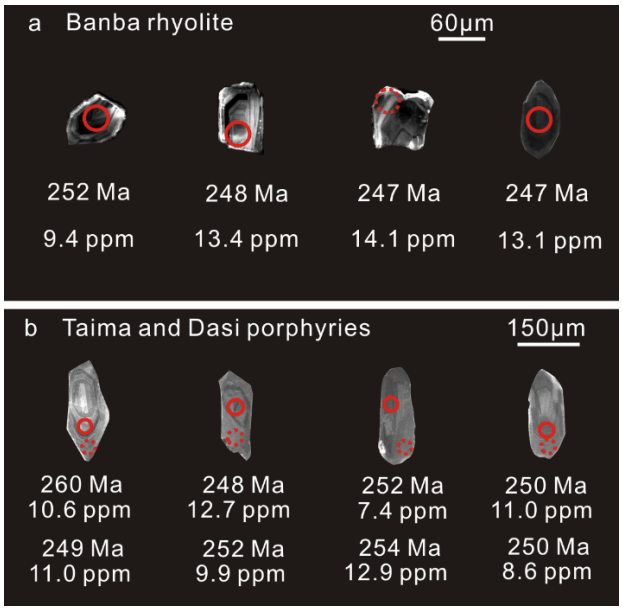

Fig. S3 Zircon cathodoluminescence images showing the age and Ti content of the core and/or rim for the Banba rhyolite (a) and Taima and Dasi porphyries (b). The red solid and dashed circles indicate the laser spots at the core and rim, respectively.

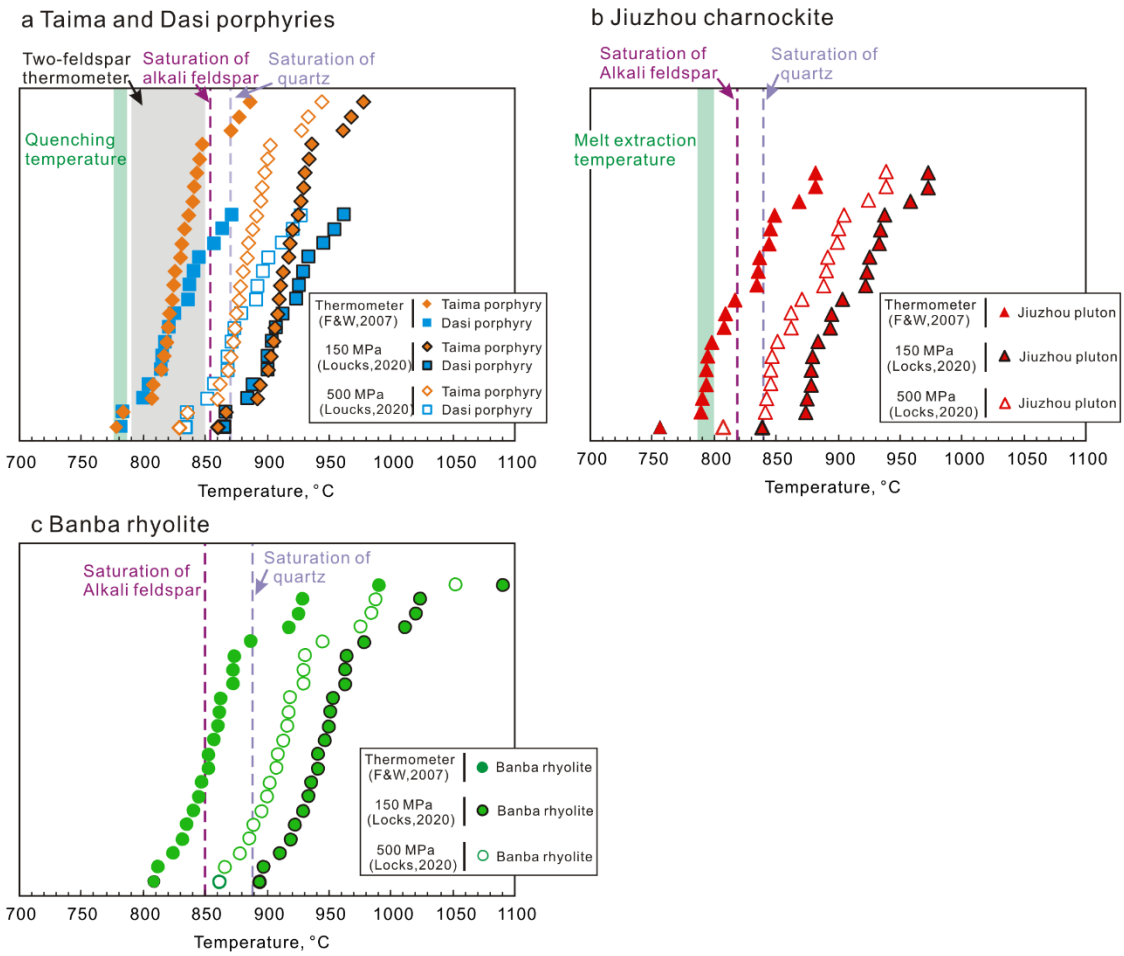

Fig. S4 Evaluation of Ti-in-zircon thermometers by Ferry and Watson (2007) and Loucks et al. (2020) using the previous temperature estimations and thermodynamic constraints for the QBGC rocks from Zhao et al. (2017a).

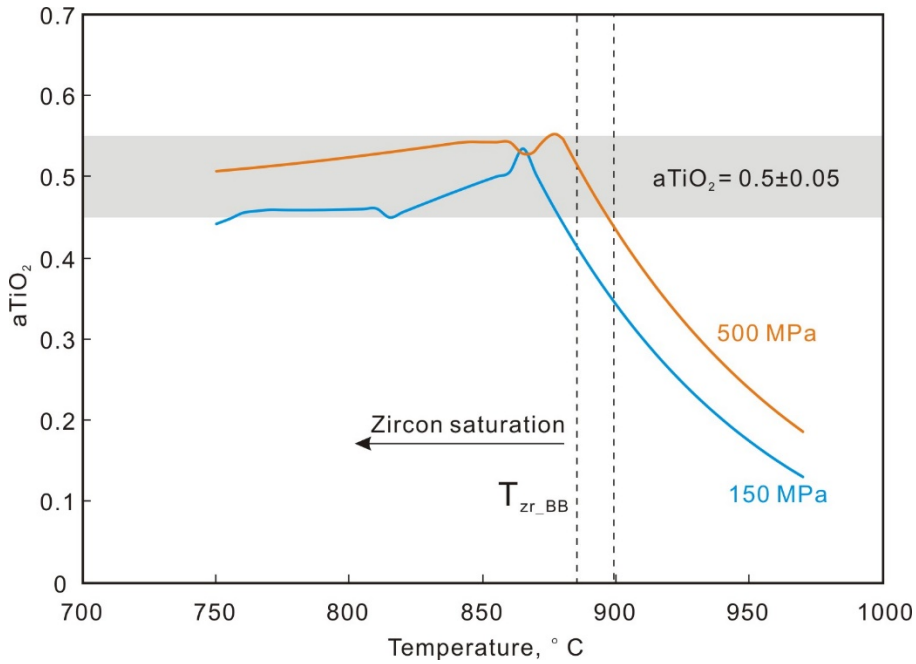

Fig. S5 Variation of $aTiO_2$ values as a function of temperature at 150 MPa and 500 MPa. $aTiO_2$ is calculated following the approach of Schiller and Finger (2019). The dashed lines denote the range of zircon saturation temperatures.

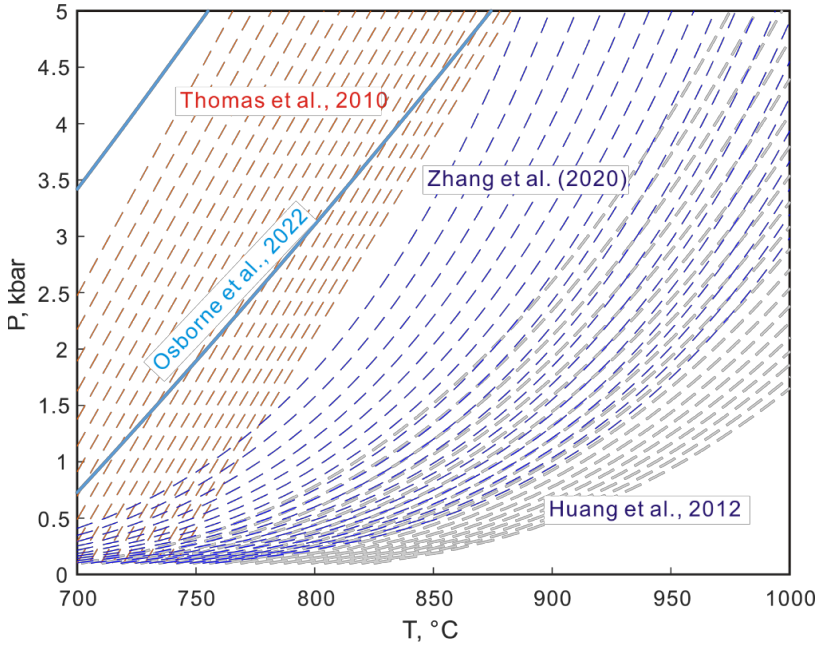

Fig. S6 Ti-in-quartz thermobarometer provides constraints on temperature and pressure conditions of magmatic processes, and here shown different experimental calibrations (Red

dashed lines, Thomas et al. 2010; Gray dashed lines, Huang et al. 2012; Blue dashed lines, Zhang et al. 2020; Bold solid lines, Osborne et al. 2022). The variation ranges of quartz Ti contents are from 150 ppm to 340 ppm.

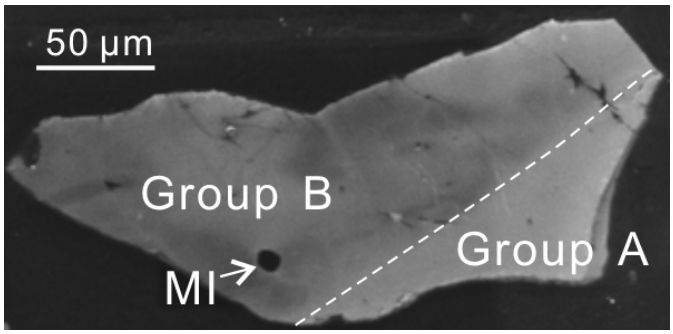

Fig. S7 CL image showing the textural relationship between quartz zonation and melt inclusion. This quartz grain containing a melt inclusion (MI) was picked up and mounted in epoxy after heating for homogenization.

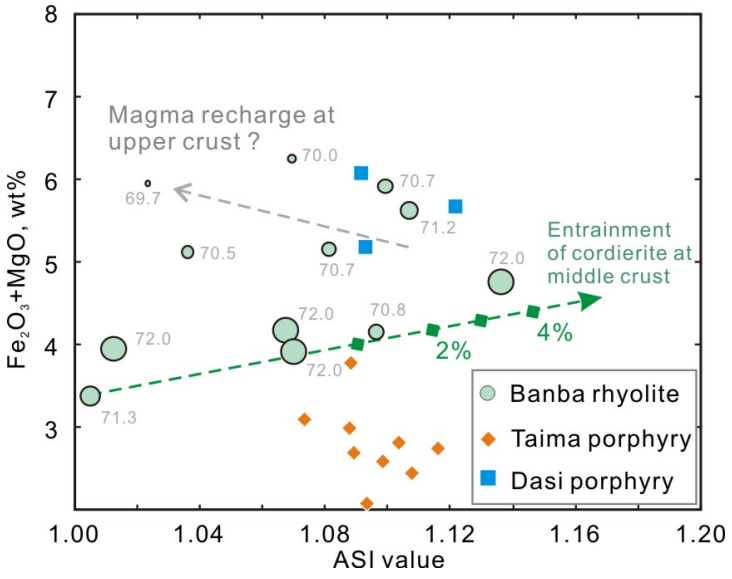

Fig. S8 Variations between ASI values and Fe_2O_3+MgO contents. SiO_2 contents (gray numbers) of the Banba rhyolites are labelled by bubble size. Green dashed arrow denotes

the modelled trend of cordierite entrainment, which can account for the large variation of ASI values (from 1.01 to 1.14) at a relatively small range of Fe_2O_3+MgO contents (from 3.4 to 4.8 wt%). Starting composition is selected to be the sample composition with lowest ASI value (~1.0). The relatively high Fe_2O_3+MgO contents (>5 wt%) and low SiO_2 contents (mostly <71 wt%) of some Banba samples are possibly caused by the mixing with recharge magmas at shallow reservoir (see details in main text). Data source is same with that of Fig. 9 in the main text.

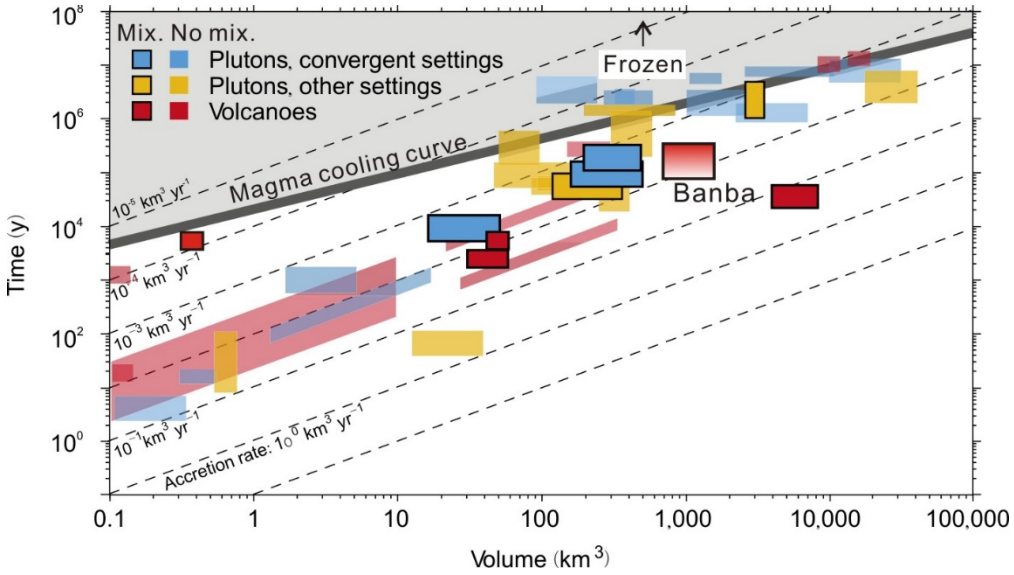

Fig. S9 Relationships between volumes of reservoir and cooling times (modified from Laumonier et al., 2014). The construction times of intrusive bodies in upper crust are compared with reservoir freezing times with volume. Thick dark curve denotes the cooling time of each reservoir size without consideration of heat input, and the shadow above the thick dark curve represents solidification of magmas as cooling dominates the thermal budget. Dashed lines give the relationship between magma flux and reservoir volume.

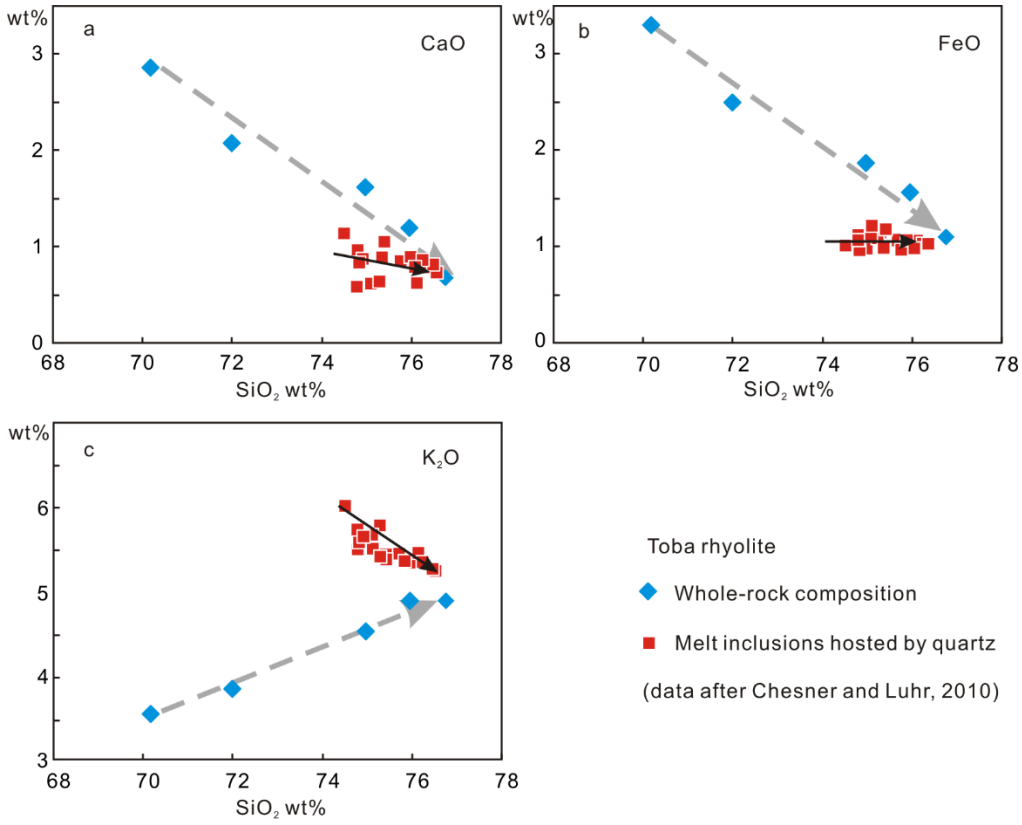

Fig. S10 Compositional variation diagrams for the Toba rhyolite, showing melt inclusion and whole rock compositions (data from Chesner and Luhr 2010). At comparable SiO_2 contents, the bulk rocks have lower K_2O contents but higher FeO and CaO contents than the melt inclusions. This feature is similar to the case of the Banba rhyolite (see more in main text).

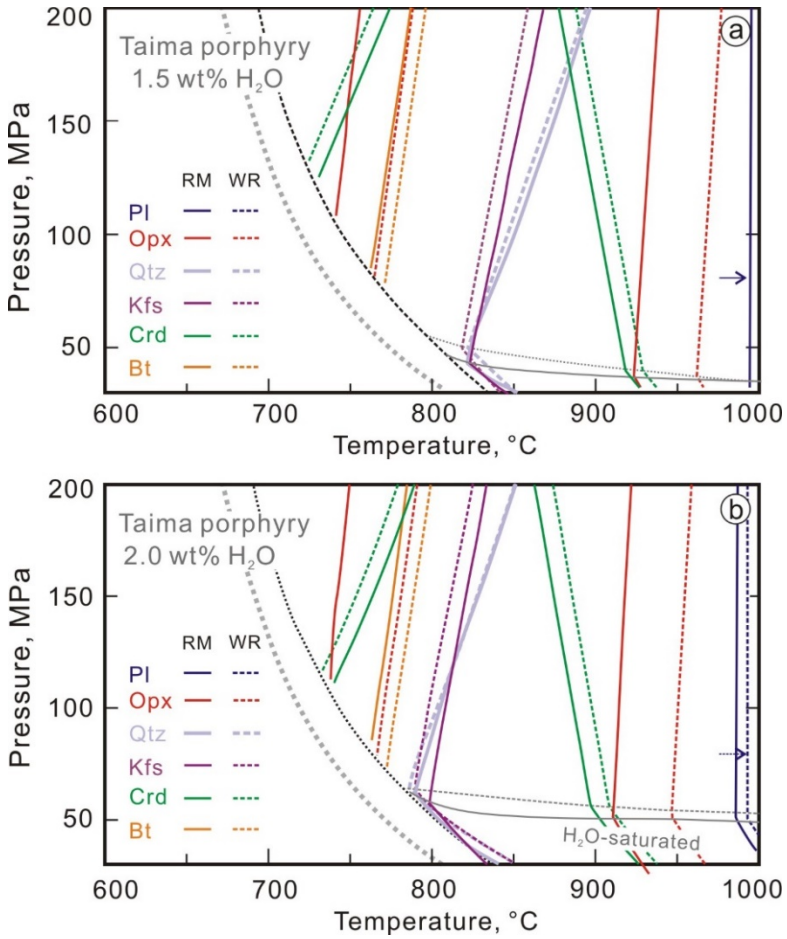

Fig. S11 Comparison of the modeled phase relations using the reactive magma (RM, solid lines; with ~71.0 wt% SiO_2) and whole-rock (WR, dashed lines; with ~72.3 wt% SiO_2) compositions for the Taima porphyry. The modeling is conducted at 1.5 wt% (a) and 2.0 wt% (b) initial H_2O contents.

Table S1 Reconstructed compositions for the reactive magmas of the Banba and Taima systems.

	Quartz	Plagioclase (An_{50})	Plagioclase (An_{60})	Average Banba (BB) rhyolite	*Reconstructed subsystem (BB) (25% OEPs, An_{50})	Reconstructed subsystem (BB) (25% OEPs, An_{60})	Reconstructed subsystem (BB) (50% OEPs, An_{50})	Average Taima (TM) porphyry	*Reconstructed subsystem (TM) (20% OEPs, An_{50})
SiO_2	100	55.29	52.06	71.33	71.26	71.33	71.18	72.31	71.00
TiO_2	-	0.003	0.03	0.56	0.59	0.59	0.61	0.36	0.60
Al_2O_3	-	27.68	30.30	12.98	12.84	12.78	12.68	14.32	12.91
Fe_2O_3	-	0.56	0.06	4.23	4.38	4.39	4.54	2.23	4.45
MnO	-	-	-	0.23	0.24	0.24	0.25	0.03	0.03
MgO	-	-	0.06	0.73	0.76	0.76	0.79	0.57	0.78
CaO	-	10.14	11.77	1.54	1.37	1.33	1.18	2.03	1.34
Na_2O	-	5.27	4.30	2.18	2.14	2.16	2.10	2.41	2.15
K_2O	-	0.41	0.45	5.00	5.18	5.18	5.38	4.97	5.27

Note: Phenocryst assemblage of the Banba rhyolite consists of <5.5 vol% quartz, <9.1 vol% plagioclase, and <4.9 vol% cordierite; Phenocryst assemblage of the Taima porphyry consists of, on average, ~13.7 vol% quartz, ~8.9 vol% alkali feldspar, ~13.6 vol% plagioclase, ~0.4 vol% biotite, ~1.84 vol% cordierite, and ~0.8 vol% orthopyroxene (data after modal analyses of nine samples). Asterisks (*) denote the reactive magmas used in thermodynamic modelling for the Banba and Taima systems.

References

Audétat, A., Miyajima, N., Wiesner, D., and Audinot, J.N. (2021) Confirmation of slow Ti diffusion in quartz by diffusion couple experiments and evidence from natural samples. Geology, 49(8), 963-967.

Barbee, O., Chesner, C., and Deering, C. (2020) Quartz crystals in Toba rhyolites show textures symptomatic of rapid crystallization. American Mineralogist, 105(2), 194-226.

Bindeman, I. (2008) Oxygen Isotopes in Mantle and Crustal Magmas as Revealed by Single Crystal Analysis. Reviews in Mineralogy and Geochemistry, 69(1), 445-478.

Chamberlain, K.J., Wilson, C.J.N., Wallace, P.J., and Millet, M.A. (2015) Micro-analytical Perspectives on the Bishop Tuff and its Magma Chamber. Journal of Petrology, 56(3), 605-640.

Cherniak, D.J., Watson, E.B., and Wark, D.A. (2007) Ti diffusion in quartz. Chemical Geology, 236(1-2), 65-74.

Chesner, C.A., and Luhr, J.F. (2010) A melt inclusion study of the Toba Tuffs, Sumatra, Indonesia. Journal of Volcanology and Geothermal Research, 197(1-4), 259-278.

Costa, F., Dohmen, R., and Chakraborty, S. (2008) Time Scales of Magmatic Processes from Modeling the Zoning Patterns of Crystals. Reviews in Mineralogy and Geochemistry, 69(1), 545-594.

Farina, F. Mayne, M.J., Stevens, G., Soorajlal, R., Frei, D. and Gerdes, A. (2020). Phase equilibria constraints on crystallization differentiation: insights into the petrogenesis of the normally zoned Buddusò Pluton in north-central Sardinia. In: Janoušek V Bonin, B., Collins WJ, Farina F, Bowden P, (eds) 2020. Post-Archean Granitic Rocks:

Petrogenetic Processes and Tectonic Environments. *Geological Society, London, Special Publications*, 491, 1, 243-265. doi.org/10.1144/SP491-2019-37.

Ferry, J.M., and Watson, E.B. (2007) New thermodynamic models and revised calibrations for the Ti-in-zircon and Zr-in-rutile thermometers. Contributions to Mineralogy and Petrology, 154(4), 429-437.

Gualda, G.A., Ghiorso, M.S., Lemons, R.V., and Carley, T.L. (2012a) Rhyolite-MELTS: a Modified Calibration of MELTS Optimized for Silica-rich, Fluid-bearing Magmatic Systems. Journal of Petrology, 53(5), 875-890.

Gualda, G.A., Pamukcu, A.S., Ghiorso, M.S., Anderson, A.T., Jr., Sutton, S.R., and Rivers, M.L. (2012b) Timescales of quartz crystallization and the longevity of the Bishop giant magma body. PLoS One, 7(5), e37492.

Huang, R., and Audétat, A. (2012) The titanium-in-quartz (TitaniQ) thermobarometer: A critical examination and re-calibration. Geochimica et Cosmochimica Acta, 84, 75-89.

Jollands, M.C., Bloch, E., and Müntener, O. (2020) New Ti-in-quartz diffusivities reconcile natural Ti zoning with time scales and temperatures of upper crustal magma reservoirs. Geology, 48(7), 654-657.

Lackey, J.S., Valley, J.W., Chen, J.H., and Stockli, D.F. (2008) Dynamic Magma Systems, Crustal Recycling, and Alteration in the Central Sierra Nevada Batholith: the Oxygen Isotope Record. Journal of Petrology, 49(7), 1397-1426.

Laumonier, M., Scaillet, B., Pichavant, M., Champallier, R., Andujar, J., and Arbaret, L. (2014) On the conditions of magma mixing and its bearing on andesite production in the crust. Nature Communications, 5, 5607.

Loucks, R.R., Fiorentini, M.L., and Henríquez, G.J. (2020) New Magmatic Oxybarometer Using Trace Elements in Zircon. Journal of Petrology, 61(3).

Osborne, Z.R., Thomas, J.B., Nachlas, W.O., Angel, R.J., Hoff, C.M., and Watson, E.B. (2022) TitaniQ revisited: expanded and improved Ti-in-quartz solubility model for thermobarometry. Contributions to Mineralogy and Petrology, 177(3).

Pearce, N.J.G., Perkins, W.T., Westgate, J.A., Gorton, M.P., Jackson, S.E., Neal, C.R., and Chenery, S.P. (1997) A Compilation of New and Published Ma j o r and Trace Element Data for NIST SRM 610 and NIST SRM 612 Glass Reference Materials. Geostandards Newsletter, 21, 115–144.

Qin, X.F., Wang, Z.Q., Zhang, Y.L., Pan, L.Z., Hu, G.A., and Zhou, F.S. (2011) Geochronology and geochemistry of Early Mesozoic acid volcanic rocks from Southwest Guangxi: Constraints on tectonic evolution of the southwestern segment of QinzhouHangzhou joint belt. Acta Petrologica Sinica, 27(3), 794-808.

Sauer, T. (2011). Numerical Analysis. Pearson USA.

Schiller, D., and Finger, F. (2019) Application of Ti-in-zircon thermometry to granite studies: problems and possible solutions. Contributions to Mineralogy and Petrology, 174(6), 51.

Student, J., J., and Bodnar, R.J. (1999) Synthetic Fluid Inclusions XIV: Coexisting Silicate Melt and Aqueous Fluid Inclusions in the Haplogranite–H_2O–NaCl–KCl System. Journal of Petrology, 40(10), 1509–1525.

Student, J.J., and Bodnar, R.J. (2004) Silicate melt inclusions in porphry copper deposit. The Canadian Mineralogist, 42, 1583-1599

Tavazzani, L., Peres, S., Sinigoi, S., Demarchi, G., Economos, R.C., and Quick, J.E. (2020) Timescales and Mechanisms of Crystal-mush Rejuvenation and Melt Extraction Recorded in Permian Plutonic and Volcanic Rocks of the Sesia Magmatic System (Southern Alps, Italy). Journal of Petrology, 61(5).

Thomas, J.B., Bruce Watson, E., Spear, F.S., Shemella, P.T., Nayak, S.K., and Lanzirotti, A. (2010) TitaniQ under pressure: the effect of pressure and temperature on the solubility of Ti in quartz. Contributions to Mineralogy and Petrology, 160(5), 743-759.

Wu, L.-G., Li, Y., Jollands, M.C., Vermeesch, P., and Li, X.-H. (2022) Diffuser: A user-friendly program for diffusion chronometry with robust uncertainty estimation. Computers & Geosciences, 163.

Zhang, C., Li, X., Almeev, R.R., Horn, I., Behrens, H., and Holtz, F. (2020) Ti-in-quartz thermobarometry and TiO_2 solubility in rhyolitic melts: New experiments and parametrization. Earth and Planetary Science Letters, 538.

Zhao, K., Xu, X., and Erdmann, S. (2017a) Crystallization conditions of peraluminous charnockites: constraints from mineral thermometry and thermodynamic modelling. Contributions to Mineralogy and Petrology, 172(5).

Zhao, K., Xu, X., and Erdmann, S. (2018) Thermodynamic modeling for an incrementally fractionated granite magma system: Implications for the origin of igneous charnockite. Earth and Planetary Science Letters, 499, 230-242.

Zhao, K., Xu, X., Erdmann, S., Liu, L., and Xia, Y. (2017b) Rapid migration of a magma source from mid- to deep-crustal levels: Insights from restitic granulite enclaves and anatectic granite. GSA Bulletin, 129, 1708–1725.

Zhao, Z.F., and Zheng, Y.F. (2003) Calculation of oxygen isotope fractionation in magmatic rocks. Chemical Geology, 193, 59–80.